Theor Chim Acta (1994) 89: 383–399

Theoretica Chimica Acta

Fourier analysis, correlation functions and nonadiabatic electron transfer: Wavepackets and exact representations

Audrey Dell Hammerich*, Abraham Nitzan, Mark A. Ratner**
Department of Chemistry, Northwestern University, Evanston, IL 60208, USA

Received June 10, 1994/Final revision received August 15, 1994/Accepted August 30, 1994

Summary. We investigate the validity of several common approximations in the analysis of nonadiabatic intramolecular electron transfer rate constants. Utilizing the Fourier representation of the golden rule form, we study the evolution of the vibrational correlation function that represents the density-of-states-weighted Franck–Condon factor. In particular, we test the validity of the perturbation theoretic golden rule form and of the Gaussian wavepacket representation for the vibrational wavefunctions against numerically exact quantum mechanical propagations. Although specific cases are found in which both of these break down, for a wide range of conditions (including anharmonic behavior and frequency changes), both the Gaussian wavepacket representation and the golden rule are excellent approximations.

Key words: Electron transfer – Nonadiabatic – Correlation functions – Propagation

1. Introduction

With his usual economy and elegance, Jan Linderberg was one of the earliest theoretical chemists to stress the importance of correlation functions, of spectral representations, and of semiclassical theory [1]. All of these have, over the past two decades, become extremely important in theoretical analysis of spectroscopic and rate processes in chemistry. Starting from ideas very similar to those of linear response as developed by Kubo [2], Gordon [3] and Heller [4] introduced into chemistry the very convenient analysis in terms of time-dependent correlation functions. While the early work was largely limited to spectroscopy, subsequent extension has also permitted application to rate phenomena [5–11, 41, 42], including (in particular) proton and electron transfer.

* *Current address*: Department of Chemistry , University of Illinois at Chicago, Chicago, IL 60607-7061, USA

** *Permanent address*: School of Chemistry, Sackler Faculty of Science, Tel Aviv University, Tel Aviv 69978, Israel

Another very important trend in current theoretical chemistry (and, again, one that Jan Linderberg has participated in from the beginning [12]) is the use of numerical representations and quasi-spectral methods to solve for the quantum dynamics of small systems [13–15]. Introduction of such grid techniques, in particular by Kosloff [13, 14], has allowed chemists to analyze the time dependence of small-molecule processes exactly, and thereby to understand some of the intimate details of short-time dynamical phenomena in chemistry.

In this paper, we utilize these numerically exact quantum dynamic analyses to investigate some generalities of nonadiabatic intramolecular electron transfers [16–24]. Using simple few-mode model systems, we test two of the most important approximations used in the time-dependent analysis of electron transfer rates, the applicability of the golden rule form and the limitations of simple Gaussian wavepacket representations for the vibrational levels. We find, in general, that for a broad range of cases both of these approximations are excellent; this is important, since they lead to particularly convenient and tractable representations for dynamical computation of vibrational effects (including dephasing, energy relaxation, and tunneling) in an electron transfer reaction.

Electron transfer rate phenomena are determined by a very broad range of physical effects, of which only the most important (vibrationally modulated electronic state mixing) are dealt within this contribution. Effects such as solvent dynamics, solvent and slow mode gating, counterion control and specific solvation are also very important [16–28]; while many of them can be treated within the general analytical schemes presented here, to do so goes beyond the scope of the current effort.

In Sect. 2, we present a very brief overview of standard nonadiabatic electron transfer theory. Section 3 overviews the correlation function/Fourier representation picture for electron transfer rates, and discusses both the golden rule approximation and the approximation of using a Gaussian wavepacket representation in contrast to the numerically exact quantum grid propagation. The core of the current paper in Sect. 4, in which these approximations are tested for some simple few-mode examples of intramolecular electron transfer reactions. Finally, comments are made in Sect. 5.

2. Intramolecular nonadiabatic electron transfer: An overview of standard rate approaches

The simplest understandings of nonadiabatic electron transfer reactions are based on the transition state model, as originally developed by Marcus [16, 17, 29]. The simple picture ignores nuclear tunneling, and equates the rate of electron transfer to the activated complex expression that would result from a coupling of two harmonic potential surfaces. Referring to Fig. 1, we define by ΔG^0 the exoergicity, or overall reaction free energy, the difference between the origins of the free energy curves corresponding to product and reactant. Along any given mode (for present purposes this can be understood simply as a normal coordinate, either of the intramolecular vibrations or of the solvent, the latter considered as a polarizable continuum or a set of phonon-like modes), we take the potential surfaces as simply two parabolas, the one on the left representing the reactant, the one on the right the product. The so-called reorganization energy along this mode, denoted by λ_i, is the energy of the product curve, relative to its own origin, at the geometry of the minimum on the reactant curve. Utilizing the definitions of ΔG^0 and λ_i as given in

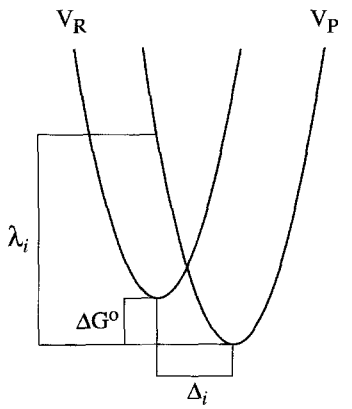

Fig. 1. Schematic view of the free energy surface along the ith normal mode defining the reorganization energy λ_i, its displacement Δ_i, and the reaction free energy ΔG^0

Fig. 1, it is a simple algebraic exercise to show that the activation energy between the minimum reactant and the (slightly avoided) curve crossing is

$$E_A = \frac{(\Delta G^0 + \lambda_i)^2}{4\lambda_i}. \tag{1}$$

In case of several degrees of freedom, the total reorganization energy is just a sum

$$\lambda = \sum_i \lambda_i, \tag{2}$$

and when substituted into a standard activated complex theory, this yields for the rate constant of electron transfer

$$k = k_0 e^{-(\Delta G^0 + \lambda)^2/4\lambda k_B T} \tag{3}$$

with k, k_0, and k_B, respectively the rate constant, frequency prefactor, and Boltzmann constant.

For nonadiabatic electron transfers, simple curve crossing analysis gives [18], to the lowest order in a curve crossing, the standard Marcus nonadiabatic electron transfer rate expression

$$k_M = \frac{V^2}{\hbar}\left(\frac{\pi}{\lambda k_B T}\right)^{1/2} e^{-(\Delta G^0 + \lambda)^2/4\lambda k_B T}. \tag{4}$$

Here V is the nonadiabatic electron transfer matrix element that corresponds to half the splitting of the reactant and product adiabatic surfaces, at the point of curve crossing. A more precise definition is given in Eq. (6) below. This Marcus result has proven both accurate and useful for an enormous number of applications in nonadiabatic electron transfers, including in particular the prediction of so-called "inverted regime behavior", for which the exoergicity exceeds the reorganization energy, and the rate is then predicted (and observed) to decrease with increasing driving force [30].

Many generalizations and extensions of the Marcus model have been produced over the years, many by Marcus himself [31]. Particularly useful early analyses were given by Jortner [24] and by Fischer and van Duyne [23] based on the use of spin-boson pictures and correlation function rate expressions. These analytic approaches yield, using steepest descent analysis to characterize the energy flow [22–24], semi-analytic expressions for the rate constant. More recently, the same

approach has been used in calculations of rate constants, with the specific time-dependent analysis of the correlation function for nuclear motion [5–7], following the scheme first suggested by Heller for spectroscopy [4].

3. Nonadiabatic electron transfer rate constant: Golden rule expressions and wavepacket representations

3.1. Coupled surface diabatic formulation

Complete analyses of the spin-boson representation for nonadiabatic electron transfer can be found in several places [20–24]. For clarity, we restrict ourselves here to a simple overview and generalize the model to allow for arbitrary vibrational motion. Following the general treatment of Marcus and the spirit of the spin-boson model, in the electron transfer event being considered only two electronic states are relevant to the problem. Figure 1 represents a cut along one of the normal coordinates of the multidimensional potential energy surface. The wavefunction for this system, expressed as a sum of products of wavefunctions for the nuclear and electronic degrees of freedom is

$$\Psi = \Psi_R |e_R\rangle + \Psi_P |e_P\rangle, \tag{5}$$

where $|e_i\rangle$ represents the electronic wavefunction for the ith potential surface. The participation of two states signifies that the simple adiabatic Born–Oppenheimer formulation is an inadequate model. By choosing a diabatic representation and integrating over the electronic degrees of freedom, the dynamics can be based upon the following coupled equations for nuclear motion which govern the amplitudes upon the reactant and product electronic potential energy surfaces:

$$i\hbar \frac{\partial \Psi_R}{\partial t} = \hat{H}_R \Psi_R + \langle e_R | \hat{V} | e_P \rangle \Psi_P, \tag{6}$$

$$i\hbar \frac{\partial \Psi_P}{\partial t} = \hat{H}_P \Psi_P + \langle e_P | \hat{V} | e_R \rangle \Psi_R.$$

The above equations assume potential couplings between the reactant and the product electronic surfaces. The Hamiltonian for the ith surface is $\hat{H}_i = \hat{T}_i + \hat{V}_i$ with $\hat{T}_i$ denoting the kinetic energy operator and $\hat{V}_i$ the potential operator. The potential coupling element corresponding to a transition from surface i to surface j is given by $\hat{V}_{ij} = \langle e_j | \hat{V} | e_i \rangle$.

With the formulation of Eq. (6), the electron transfer dynamics can be solved. Choosing a normal coordinate representation for each mode (ignoring all anharmonicities) considerably simplifies the Hamiltonian operation as each surface Hamiltonian is then completely separable. The only coupling which remains is the potential coupling between the electronic surfaces responsible for the electron transfer rate or the back electron transfer rate after photoabsorption within the charge transfer (CT) band. Thus, the analysis requires propagation of nuclear wavefunctions for which a number of techniques are available [13, 14]. The wavefunction for the initial state is determined by an imaginary time relaxation procedure on the relevant electronic potential energy surface [32]. With this initial wavefunction the equations of motion are integrated by a short iterative Lanczos (SIL) scheme [15, 33]. When only the electron transfer rate is desired, propagation

can alternatively be performed with a Chebychev expansion of the evolution operator adapted for short-time calculation of autocorrelation functions [13]. A fourth-order Runge–Kutta scheme is employed to integrate the Gaussian wavepacket parameters.

3.2. *Electron transfer process*

From the equations of motion given in Eq. (6) the change in the population on a surface can be determined

$$\frac{\mathrm{d}}{\mathrm{d}t}\langle\Psi_{\mathrm{R}}(t)|\Psi_{\mathrm{R}}(t)\rangle = \frac{2}{\hbar}\,\mathrm{Im}[\langle\Psi_{\mathrm{R}}(t)|\hat{V}_{\mathrm{RP}}|\Psi_{\mathrm{P}}(t)\rangle],$$

$$\frac{\mathrm{d}}{\mathrm{d}t}\langle\Psi_{\mathrm{P}}(t)|\Psi_{\mathrm{P}}(t)\rangle = -\frac{2}{\hbar}\,\mathrm{Im}[\langle\Psi_{\mathrm{R}}(t)|\hat{V}_{\mathrm{RP}}|\Psi_{\mathrm{P}}(t)\rangle]. \tag{7}$$

The time derivative of the normalization is recognized as the transition probability per unit time or the instantaneous rate. A time-dependent potential coupling [8] defines the nonadiabatic coupling process which characterizes the electron transfer event

$$V_{\mathrm{RP}}(t) = \langle\Psi_{\mathrm{R}}(t)|\hat{V}_{\mathrm{RP}}|\Psi_{\mathrm{P}}(t)\rangle. \tag{8}$$

Then the instantaneous rate is given by the imaginary part of the time-dependent potential coupling

$$\Gamma_{\mathrm{e}}(t) = -\frac{\mathrm{d}}{\mathrm{d}t}\langle\Psi_{\mathrm{R}}(t)|\Psi_{\mathrm{R}}(t)\rangle = -\frac{2}{\hbar}\,\mathrm{Im}[V_{\mathrm{RP}}(t)]. \tag{9}$$

To obtain a more transparent expression for the rate, consider the formal exact solution to Eq. (6) where the lower limit of integration is set to the origin of time for the experiment and the process being simulated:

$$\Psi_{\mathrm{R}}(t) = \mathrm{e}^{-\mathrm{i}\hat{H}_{\mathrm{R}}t/\hbar}\Psi_{\mathrm{R}}(0) - \frac{\mathrm{i}}{\hbar}\int_0^t \mathrm{d}t'\,\mathrm{e}^{-\mathrm{i}\hat{H}_{\mathrm{R}}(t-t')/\hbar}\,\hat{V}_{\mathrm{RP}}\Psi_{\mathrm{P}}(t'),$$

$$\Psi_{\mathrm{P}}(t) = \mathrm{e}^{-\mathrm{i}\hat{H}_{\mathrm{P}}t/\hbar}\Psi_{\mathrm{P}}(0) - \frac{\mathrm{i}}{\hbar}\int_0^t \mathrm{d}t'\,\mathrm{e}^{-\mathrm{i}\hat{H}_{\mathrm{P}}(t-t')/\hbar}\,\hat{V}_{\mathrm{PR}}\Psi_{\mathrm{R}}(t'). \tag{10}$$

The electron transfer process assumes that no amplitude is originally present on the product electronic surface so that only the second term for $\Psi_{\mathrm{P}}(t)$ is retained in Eq. (10). Then

$$\Gamma_{\mathrm{e}}(t) = \frac{2}{\hbar^2}\,\mathrm{Re}\left[\int_0^t \mathrm{d}t'\langle\Psi_{\mathrm{R}}(t)|\hat{V}_{\mathrm{RP}}\mathrm{e}^{-\mathrm{i}\hat{H}_{\mathrm{P}}(t-t')/\hbar}\,\hat{V}_{\mathrm{PR}}|\Psi_{\mathrm{R}}(t')\rangle\right]. \tag{11}$$

Equation (11) specifies an instantaneous value for the electron transfer rate constant. However, no experiment can determine an instantaneous rate. All real detection systems observe a signal that is integrated over a characteristic time interval. This is perfectly in keeping with the notion that rate constants are truly constant and therefore independent of time. Defining a new wavefunction

$|\phi(t)\rangle = \hat{V}_{PR}|\Psi_R(t)\rangle$, the dynamics of a "potentially dressed" reactant state can be examined for some period T.

$$\Gamma_e = \langle \Gamma_e(t)\rangle_T = \frac{1}{T}\int_0^T dt\, \frac{2}{\hbar^2}\,\mathrm{Re}\left[\int_0^t dt' \langle \phi(t)|\, e^{-i\hat{H}_P(t-t')/\hbar}|\phi(t')\rangle\right]. \tag{12}$$

The electron transfer rate given by Eq. (12) is portrayed as the dynamic overlap of a nonstationary state $\phi(t)$ defining the electron localized on the reactant site (such as a donor) with its prior evolution from t' to t upon the electronic surface characteristic of the product (e.g., an acceptor) nuclear configuration. Under appropriate conditions this overlap can be taken between stationary states.

3.3. Linear response limit-golden rule

Since Eq. (12) is an exact relation, one can recover the linear response result (first order in perturbation theory) for the electron transfer rate. If the magnitude of $\hat{V}_{RP}$ is small, the potential coupling can be considered as a perturbation. Then the second term for $\Psi_R(t)$ in Eq. (10) may be neglected. Therefore, for a vibrational eigenstate of the reactant electronic surface, $\Psi_R(t) = e^{-iE_Rt/\hbar}\Psi_R(0)$. This value is inserted into the equation for $\Psi_P(t)$ in Eq. (10), yielding the amplitude to first order:

$$\Gamma_e = \frac{1}{T}\int_0^T dt\, \frac{2}{\hbar^2}\,\mathrm{Re}\left[\int_0^t dt'\, e^{-iE_Rt'/\hbar}\langle \Psi_R(0)|\hat{V}_{RP}e^{-i\hat{H}_Pt'/\hbar}\hat{V}_{PR}|\Psi_R(0)\rangle\right]. \tag{13}$$

In a time time-dependent framework the difference between the linear and nonlinear response expressions for the rate (Eqs. (13) and (12)) arises in transitions between stationary versus nonstationary reactant states. The two inner integrals over each of the complex conjugate terms combine together to yield a full finite Fourier transform in this linear response limit:

$$\Gamma_e = \frac{1}{T}\int_0^T dt\, \frac{1}{\hbar^2}\int_{-t}^t dt'\, e^{-iE_Rt'/\hbar}\langle \Phi|\Phi(t')\rangle, \tag{14}$$

where $\Phi = V_{RP}\Psi(0)$ and $\Phi(t) = e^{-i\hat{H}_Pt/\hbar}\Phi$. If the autocorrelation function, $\langle \Phi|\Phi(t')\rangle$, decays to zero at $t = \tau$, the inner integral becomes time independent for all times greater than τ and the subsequent time-averaging operation makes no contribution to the rate. Since this time-independent result is just the instantaneous rate of Eq. (9), the transition probability per unit time is also time independent, in accord with the first-order perturbation theory expression of Fermi's golden rule. The limits of integration may than be formally extended to infinity,

$$\Gamma_e = \frac{1}{\hbar^2}\int_{-\infty}^{+\infty} dt\, e^{-iE_Rt/\hbar}\langle \Phi|\Phi(t)\rangle, \tag{15}$$

to yield the standard result of linear response theory interpreted within a time-dependent wavepacket framework [3, 4]. This equivalence is best observed in the expression for the photoabsorption cross section that corresponds to the optical transition of the donor,

$$\sigma(\omega) = \frac{2\pi\omega}{3\hbar c}\int_{-\infty}^{+\infty} dt\, e^{-i(\omega + E_R/\hbar)t}\langle \chi|\chi(t)\rangle, \tag{16}$$

where now $\chi = \mu_{PR} e \Psi_R(0)$. When the potential coupling is taken to be coordinate independent (Condon approximation), aside from the prefactor, the electron transfer rate is seen to correspond to a "zero" frequency vertical optical transition. A similar parallel exists for the charge transfer absorption.

3.4. *Vibrational representations – Gaussian wavepackets*

The correlation function expression in Eq. (15) represents vibrational motion, and can be calculated exactly using grid methods [13–15]. A number of workers [6, 7] have suggested that it should generally be adequate to replace the vibrational states in Eq. (15) by the representation in terms of Gaussian wavepackets, as given by

$$\Psi(Q, t) = \exp\left[\frac{\mathrm{i}}{\hbar} A(t)[Q - Q(t)]^2 + \mathrm{i}P(t)[Q - Q(t)] - \frac{\mathrm{i}}{\hbar} G(t)\right] \tag{17}$$

for a particular mode Q. The variables $Q(t)$, $P(t)$, $A(t)$, and $G(t)$ denote the dimensionless coordinate, momentum, width, and phase of the Gaussian wavepacket, respectively. Their time evolution follows from equations of motion given by Heller [4]

$$\begin{aligned}
\frac{\mathrm{d}Q(t)}{\mathrm{d}t} &= \omega P(t), \\
\frac{\mathrm{d}P(t)}{\mathrm{d}t} &= -\frac{1}{\hbar}\frac{\partial V}{\partial Q}\bigg|_{Q=Q(t)}, \\
\frac{\mathrm{d}A(t)}{\mathrm{d}t} &= -\frac{2\omega}{\hbar} A^2(t) - \frac{1}{2}\frac{\partial^2 V}{\partial Q^2}\bigg|_{Q=Q(t)}, \\
\frac{\mathrm{d}G(t)}{\mathrm{d}t} &= \hbar\omega P^2(t) + \mathrm{i}\omega A(t) - E,
\end{aligned} \tag{18}$$

where V (which will be either V_R or V_P) denotes the potential for vibrational motion for the Qth mode. The frozen Gaussian approximation results when $A(t) =$ constant in Eq. (18).

Nitzan and Neria [6] have argued, and demonstrated, that in the very short times generally involved in the meaningful evolution of Eq. (15) (generally less than 50 fs), there is not really time for the Gaussian wavepackets to spread, and therefore that use of frozen packets with appropriate widths will give an excellent approximation for the evolution of the correlation function. They tested this by analysis of two limits for a harmonic oscillator, one where the product state is another identical displaced oscillator, and the second where the product state is simply a dissociative linear potential. One aim of the current paper is to test the validity of the Gaussian and frozen Gaussian approximations by comparison with exact propagations.

The golden rule result of Eq. (15) is, itself, based on truncation of the equations of motion given in Eq. (10) assuming a small mixing coefficient $\hat{V}$. More generally, one can simply solve the equations exactly yielding Eq. (12). When these equations are solved to lowest order in $\hat{V}$, one recovers the golden rule expression of Eq. (15). The second aim of the current paper is to test the validity, in particular simple models, of the golden rule expression.

4. Applicability of the golden rule and Gaussian wavepackets

4.1. Gaussian wavepackets

Gaussian wavepackets are often employed to represent the vibrational motion when calculating intramolecular electron transfer rate constants. Furthermore, the Gaussians are generally taken to be "frozen" so that their widths do not change during their evolution. These approximations are predicated upon the assumption that the autocorrelation function of Eq. (15) decays rapidly. This point is examined for a few simple models where there is a frequency change between the reactant and product potential surfaces and for varying degrees of anharmonicity.

The first example for examining Gaussian wavepacket representations is drawn from the class of symmetric outer-sphere electron transfer reactions. The self-exchange of hexaaquoiron (II)/hexaaquoiron (III)

$$Fe^{II}(H_2O)_6 + Fe^{III}(H_2O)_6 \rightarrow Fe^{III}(H_2O)_6 + Fe^{II}(H_2O)_6 \qquad (19)$$

has become a prototype for understanding electron transfer [34, 35]. To examine this system, we employed the model of Siders and Marcus [35] which approximates the frequency dispersion of the aqueous solvent by two frequencies (1 and 170 cm^{-1}). The internal reorganization energy was attributed to an averaged metal–oxygen symmetrical stretching frequency of 431 cm^{-1}. For computational simplicity in the quantum grid method, the 1 cm^{-1} mode was replaced by a 20 cm^{-1} mode, with the same reorganization energy. Table 1 gives the parameters employed based upon a 0.14 Å change in equilibrium bond length [36] and an averaged force constant [37].

Figure 2 gives the real part of the autocorrelation function of Eq. (15) as a function of time for three different Gaussian propagations. The solid line denotes the correlation function when an average frequency of 431 cm^{-1} is used to represent the symmetrical stretching frequency of the metal ligand bond. The dotted and dashed curves are the respective frozen and thawed Gaussian wavepacket propagations, when separate breathing frequencies of 389 and 490 cm^{-1} are used for $Fe^{II}(H_2O)_6$ and $Fe^{III}(H_2O)_6$, respectively. While a slight difference is observed between the use of an average frequency versus two separate frequencies, no discernible difference can be seen between the frozen and thawed Gaussian propagations. The Gaussian propagations are correct; Fig. 3 compares a (thawed) Gaussian propagation for this system denoted by the dotted curve with an exact calculation given by the solid curve. The slight difference in the autocorrelation function results in Fig. 2 are mirrored in the rate constant. Figure 4 shows the rate constant as a function of $-\Delta G^0$. The small difference in the peak maxima, which define the crossing point into the inverted region, between the solid curve (average frequency) and the others (separate frequencies) arises since the potential surfaces is not cylindrically symmetric with respect to the reaction coordinate in bond displacement with the two separate frequencies as it is for the single frequency [34].

Since the symmetrical stretching (breathing) model of the metal ligand bond is quite different for the Fe^{II} and Fe^{III} centres (389 and 490 cm^{-1}, respectively), the effect of employing an average frequency of 431 cm^{-1} may have been anticipated to be larger, especially with respect to "frozen" versus "thawed" Gaussian wavepacket propagations. Even though the Fe^{II}/Fe^{III} system possesses substantial internal reorganization energy and a 100 m^{-1} shift is significant, in examining Figs. 2 and 4, little effect is seen upon either the autocorrelation function or the rate constant.

Table 1. Model parameters

	Δ	λ	
$Fe^{III}(H_2O)_6 + Fe^{II}(H_2O)_6 \rightarrow Fe^{II}(H_2O)_6 + Fe^{III}(H_2O)_6$			
$\bar{\omega} = 431$	7.36	11670	$\lambda_{in} = 11670$
$\omega_{1s} = 20$	17.5	3063	$\lambda_{out} = 9017$
$\omega_{2s} = 170$	8.37	5955	
$\omega_1 = 490 \rightarrow 389$	4.94	4747	$\lambda_{in} = 12290$
$\omega_2 = 389 \rightarrow 490$	5.55	7547	
$\omega_{1s} = 20$	17.5	3063	$\lambda_{out} = 9017$
$\omega_{2s} = 170$	8.37	5955	
$Fe^{III}(H_2O)_6 + Ru^{II}(NH_3)_6 \rightarrow Fe^{II}(H_2O)_6 + Ru^{III}(NH_3)_6$			
	Δ	λ	
$\bar{\omega}_{Fe} = 431$	5.20	5827	$\lambda_{in} = 6224$
$\bar{\omega}_{Ru} = 405$	1.40	397	
$\omega_{1s} = 20$	28.2	7952	$\lambda_{out} = 23440$
$\omega_{2s} = 170$	13.5	15490	
$\omega_{Fe} = 490 \rightarrow 389$	3.49	2369	$\lambda_{in} = 2672$
$\omega_{Ru} = 350 \rightarrow 500$	1.10	303	
$\omega_{1s} = 20$	28.2	7952	$\lambda_{out} = 23440$
$\omega_{2s} = 170$	13.5	15490	
$Co^{III}(NH_3)_6 + e^- \rightarrow Co^{II}(NH_3)_6$			
$\omega = 494 \rightarrow 357$	5.85	6109	
Nonperturbative electron transfer dynamics for 1–4 modes			
$\omega_1 = 450$	2.6	1521	1–3 modes with $\Delta G^0 = 0$
$\omega_2 = 170$	6.75	3873	
$\omega_3 = 20$	14.1	1988	
$\omega_1 = 431$	2.6	1457	4 modes with $\Delta G^0 = -2743$
$\omega_2 = 405$	0.7	99	
$\omega_3 = 170$	6.75	3873	
$\omega_4 = 20$	14.1	1988	

A similar conclusion was reached in a Gaussian wavepacket propagation for the same model [38]. The electron transfer dynamics with frozen Gaussians and an average stretching frequency were basically identical to either frozen or thawed Gaussian propagations with different frequencies. In that study it was surmised that the lack of sensitivity was due to the symmetric nature of the system where one frequency increases in consort to another's decrease.

To examine better the effect of a frequency change, we chose the unsymmetrical hexaaquiron (III)/hexaammineruthenium (II) reaction,

$$Fe^{III}(H_2O)_6 + Ru^{II}(NH_3)_6 \rightarrow Fe^{II}(H_2O)_6 + Ru^{III}(NH_3)_6. \tag{20}$$

The reorganization energies were taken to be one-half of the respective redox couple [37]. The parameters for $Ru^{II}(NH_3)_6/Ru^{III}(NH_3)_6$ and the treatment of the solvent again follow Siders and Marcus [35]. In this unsymmetrical case, though

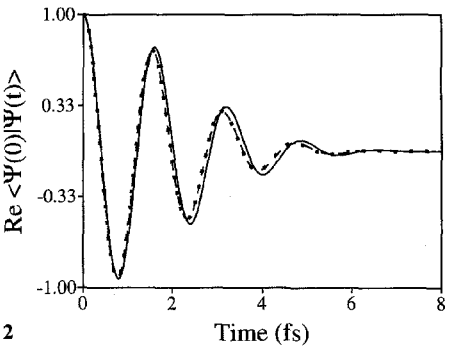
1.00
0.33
-0.33
-1.00
Re <Ψ(0)|Ψ(t)>
0
2
4
6
8
Time (fs)

2

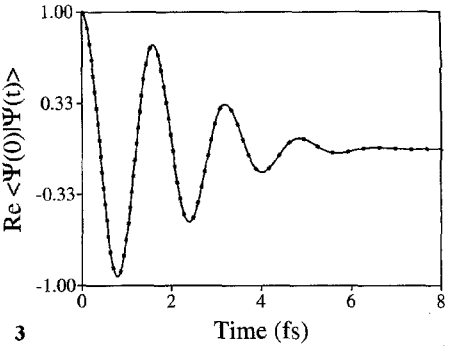
1.00
0.33
-0.33
-1.00
Re <Ψ(0)|Ψ(t)>
0
2
4
6
8
Time (fs)

3

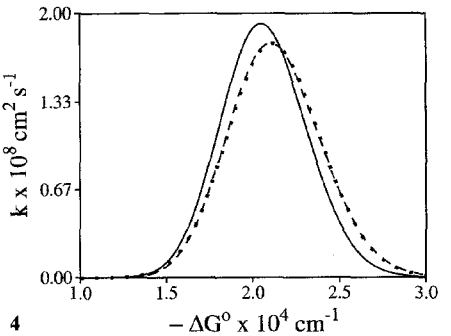
2.00
1.33
0.67
0.00
k x 10^8 cm^2 s^-1
1.0
1.5
2.0
2.5
3.0
– ΔG° x 10^4 cm^-1

4

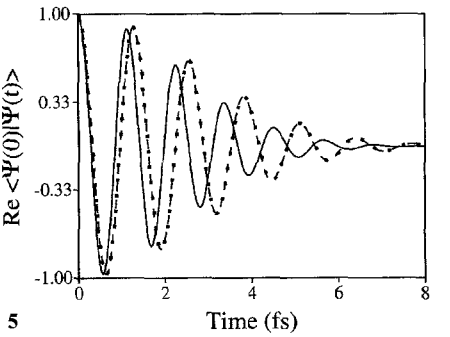
1.00
0.33
-0.33
-1.00
Re <Ψ(0)|Ψ(t)>
0
2
4
6
8
Time (fs)

5

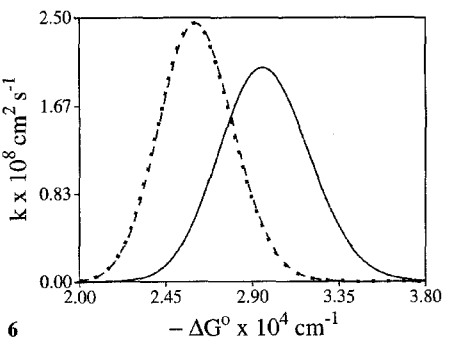
2.50
1.67
0.83
0.00
k x 10^8 cm^2 s^-1
2.00
2.45
2.90
3.35
3.80
– ΔG° x 10^4 cm^-1

6

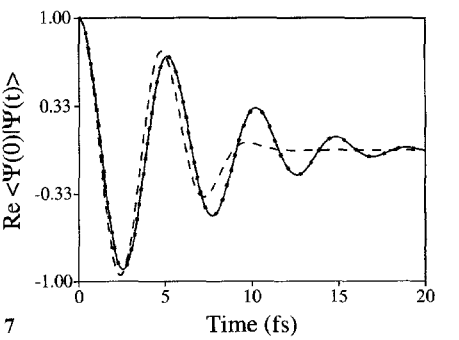
1.00
0.33
-0.33
-1.00
Re <Ψ(0)|Ψ(t)>
0
5
10
15
20
Time (fs)

7

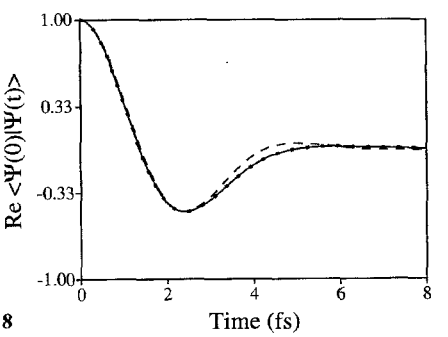
1.00
0.33
-0.33
-1.00
Re <Ψ(0)|Ψ(t)>
0
2
4
6
8
Time (fs)

8

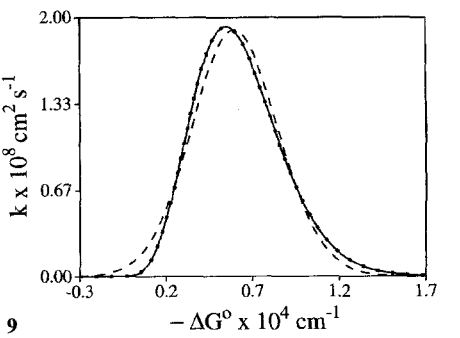
2.00
1.33
0.67
0.00
k x 10^8 cm^2 s^-1
-0.3
0.2
0.7
1.2
1.7
– ΔG° x 10^4 cm^-1

9

the ruthenium ligand frequency changes by 150 cm^{-1} (from 350 to 500 cm^{-1}), the corresponding reorganization energy is small. Therefore, the change in the iron displacement dominates the internal reorganization, and contrary to the Fe^{II}/Fe^{III} self-exchange reaction, the frequency change does not have a parallel compensation. The frequency change in this system may serve as a good test of Gaussian wavepacket propagations. Table 1 summarizes the parameters employed where a 0.04 Å change in equilibrium Ru–N bond distance is used [39].

Figure 5 portrays the autocorrelation function for the Fe/Ru reaction. The solid curve is obtained when using average stretching frequencies for both the iron and ruthenium metal ligand bonds. The dotted and dashed curves are for the respective frozen and thawed propagations with separate frequencies. In comparison to Fig. 2, a dramatic difference is encountered when employing an average frequency. The rate constant dependence is encountered when employing an average frequency. The rate constant dependence given in Fig. 6 emphasizes this point. The difference in the crossing points (rate maxima) is seen in the energy difference given in Table 1 and reflects the dominance of the Fe^{III}/Fe^{II} internal reorganization without compensation from the ruthenium couple when using separate frequencies. Yet, still, the frozen and thawed Gaussian propagations are practically identical, yielding rate constants that differ by only a few percent.

For all of the Gaussian propagations the reactant state was chosen to be a minimum uncertainty wavepacket (Glauber coherent state). When only frequency changes occur in an harmonic potential, this choice minimizes the

---

Fig. 2. Time dependence of the real part of the autocorrelation function of Eq. (15) for the $Fe^{II}(H_2O)_6/Fe^{III}(H_2O)_6$ self-exchange reaction incorporating two solvent modes. The solid line denotes a Gaussian wavepacket propagation employing an average metal ligand symmetric stretch frequency. The dotted and dashed curves denote frozen and thawed propagations, respectively, using two different frequencies corresponding to the Fe^{II} and Fe^{III} centers

Fig. 3. Comparison of the autocorrelation function obtained with a Gaussian wavepacket representation versus an exact wavepacket representation for the same system given in Fig. 2

Fig. 4. Rate constant as a function of $-\Delta G^0$ for the system given in Fig. 2. The solid curve is for an average frequency and the dotted and dashed curves depict frozen and thawed Gaussian propagations, respectively, employing two separate frequencies

Fig. 5. Time dependence of the real part of the autocorrelation function of Eq. (15) for the $Fe^{III}(H_2O)_6/Ru^{II}(NH_3)_6$ cross reaction incorporating two solvent modes. The solid line is from a Gaussian wavepacket propagation with average stretching frequencies for both Fe–O and Ru–N metal ligand bonds. Frozen and thawed Gaussian propagations are, respectively, given by the dotted and dashed curves utilizing different frequencies

Fig. 6. Rate constant as a function of $-\Delta G^0$ for the system given in Fig. 5. Solid line employs an average frequency and the dotted (frozen) and dashed (thawed) curves use separate frequencies

Fig. 7. Autocorrelation function corresponding to the reduction half reaction for $Co^{III}(NH_3)_6$. The dashed curve gives the frozen Gaussian result while the dotted and solid curves are for the thawed and exact propagations. The width of the initial reactant state is one-fourth the coherent state value

Fig. 8. The same system and propagations given in Fig. 7 except that the initial width is four times of the coherent state

Fig. 9. Rate constant as a function of $-\Delta G^0$ for the system of Fig. 8. The curves are similarly identified

difference between frozen and thawed Gaussian wavepacket propagations. So for a rapidly decaying autocorrelation function, the two different Gaussian propagations can be nearly identical as long as the potentials are harmonic. This point can be illustrated by examining situations where the width of the initial reactant state is chosen to be either narrower or broader than the width of the ground state of the harmonic oscillator.

As an illustration, the half reaction corresponding to the reduction

$$Co^{III}(NH_3)_6 + e \rightarrow Co^{II}(NH_3)_6 \tag{21}$$

is considered. Focusing upon the vibrational levels, a large effect for Gaussians of different widths may be anticipated since the frequency changes from 494 to 357 cm^{-1} with a 0.178 Å change in equilibrium metal ligand bond length between the two cobalt oxidation states [40]. The parameters employed are given in Table I. Figure 7 gives the autocorrelation function where the initial reactant width is one-fourth the minimum uncertainty width. The dashed curve corresponds to the frozen Gaussian propagation while the dotted and solid curves represent the thawed and exact propagations, respectively. Figure 8 displays parallel propagations for a width that is four times the coherent state value. This latter figure appears to suggest that it is better to err with a width that exceeds the width of the ground state harmonic oscillator wavefunction than one that is proportionately smaller. Nevertheless, an error may still result. Figure 9 represents the full energy dependency of the rate for the system given in Fig. 8. As Fig. 9 shows, the frozen Gaussian approximation overestimates the low energy tail for this case.

The fact that average breathing frequencies can be used instead of separate frequencies, with very low error, has been shown in a comprehensive examination of the hexaaquoiron self-exchange reaction [34]. When an average frequency is appropriate and the wavepacket is a coherent state, frozen Gaussian propagations are exact (for harmonic potentials). As one moves beyond self-exchange reactions with their compensating frequency increases and frequency decreases, the approximation of averaging frequencies becomes poorer. However, for short-term dynamics, little difference between frozen and thawed Gaussian propagations can be seen for these cases. If a minimum uncertainty wavepacket is not chosen for the reactant state, considerable differences can arise between these two propagations, even for harmonic potentials. One is naturally led to consider the behavior for anharmonic potentials.

In addition to its frequency and a dimensionless displacement, a Morse potential is completely defined by introducing a dimensionless energy

$$\delta^2 = \frac{\hbar\omega}{2D_e}, \tag{22}$$

so that the energy of the nth level is

$$E_n = \hbar\omega(n + \tfrac{1}{2}) - \frac{\delta^2}{2}\hbar\omega(n + \tfrac{1}{2})^2. \tag{23}$$

Realistic values of δ can range from 0.11 for I_2, 0.24 for H_2, or 0.81 for the He–I Morse potential of the van der Waals complex He/I_2. Anharmonicities will be examined for Morse potentials with varying δ's.

Returning to the Fe^{III}/Ru^{II} cross reaction, by systematically increasing δ the autocorrelation function decays proportionally faster. This has a profound effect upon the rate. Figure 10 gives the rates from thawed Gaussian propagations

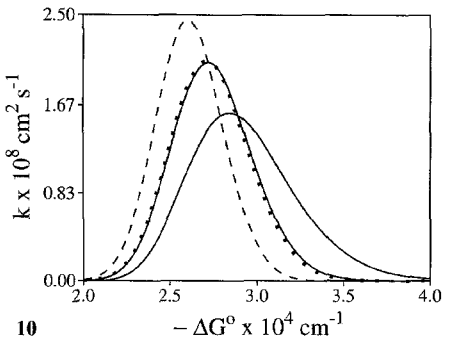

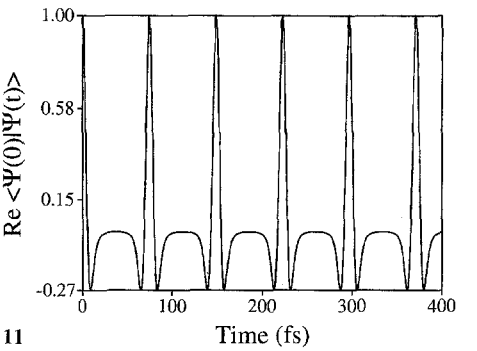

Fig. 10. Rate constant as a function of $-\Delta G^0$ for the $Fe^{III}(H_2O)_6/Ru^{II}(NH_3)_6$ cross reaction where the two solvent modes are treated as harmonic while the metal ligand modes are characterized by varying degrees of anharmonicity. Dashed: $\delta = 0$ (harmonic-no anharmonicity); dotted: $\delta = 1$; and right hand solid curve: $\delta = 2$. Left hand solid curve employs $\delta = 1$ for the low-frequency metal ligand mode and $\delta = 2$ for the high frequency mode in the Fe^{III}/Fe^{II} and Ru^{II}/Ru^{III} couples

Fig. 11. Autocorrelation function of single mode case ($\omega_1 = 450$)

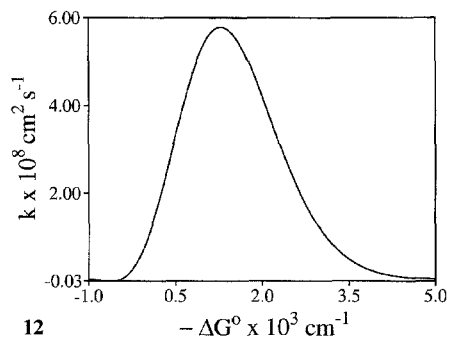

Fig. 12. Rate constant as a function of $-\Delta G^0$ for the single mode case given in Fig. 11

employing different frequencies for both the iron and ruthenium symmetric stretching modes. Two solvent modes were incorporated as given in Table 1 and are treated as harmonic. Morse potentials are applied to the metal ligand modes. The dashed rate plot is identical with the dashed curve of Fig. 6 and represents harmonic metal ligand treatment. The dotted curve is a Morse with $\delta = 0.1$ and an observed ground state frequency equivalent to the ground state harmonic. The dash-dotted curve corresponds to $\delta = 0.2$. In these two cases, the reactant and product potentials were assumed to have the same degree of anharmonicity. The solid curve considers the low-frequency modes to have $\delta = 1$ and the high-frequency modes $\delta = 2$. All cases start with a minimum uncertainty wavepacket for the reactant state whose width is allowed to vary during its propagation. Frozen Gaussians (not shown) become increasingly worse as either the level of anharmonicity increases while the observed frequency remains unchanged (the average 405 and 431 cm^{-1} values in Table 1) or the frequencies change for a given degree of anharmonicity.

4.2. *Golden rule*

Quantum mechanical treatments of electron transfer processes are based upon adiabatic or nonadiabatic approaches depending upon the magnitude of the nonadiabatic electron transfer matrix element V. The overwhelming majority of the nonadiabatic treatments are formulated within the limits of first-order perturbation theory, employing Fermi's golden rule [18]. This linear response limit greatly simplifies the theoretical development and has enjoyed considerable popularity. A major question to be answered is when is the linear response limit applicable and when does it fail [18, 19].

As a first step towards answering this question, the population transfer to products from a series of reactant states containing from one to four quantum modes is examined. The parameters defining these states are listed in Table 1. The three- and four-mode examples explicitly incorporate the previous model quantum description (a few harmonic modes) for a solvent. The equations of motion are integrated for a range of values of the nonadiabatic potential coupling. In all cases the potential coupling is taken to be constant (Condon approximation).

For the one-mode case, the perturbative rate is given by integrating the autocorrelation function shown in Fig. 11. As the figure demonstrates, in practice, the instantaneous rate experiences recurrence due to the periods of the fundamental frequencies of the bound modes of the system. This may be formally circumvented by time averaging over half a period of the oscillation between the turning points of the mode motion to yield the rate versus free energy curve of Fig. 12. The rates so obtained agree with other perturbative treatments. In contrast to the high-temperature limit rate constant of Eq. (4), here comparison is more appropriately made with a low-temperature limit. For this system, the maximum rate at the crossing point given by a polaron treatment [24] is 5.71×10^8 cm^2 s^{-1}. Figure 12 displays nearly an identical result (5.79×10^8). Note that these "rates", as those given in Figs. 4, 6, 9, and 10, need to be multiplied by the square of the nonadiabatic potential coupling in cm^{-1} in order to yield a conventional rate constant in reciprocal seconds.

Theoretical justification for ignoring the recurrences derives from the assumption that the solvent dynamics are sufficiently rapid (and disperse) to dephase the system on any relevant molecular time scale so that the autocorrelation function decays to zero before a recurrence can be reached. In essence, this overdamped solvent enforces the linear response limit. From the perspective of the autocorrelation function, the solvent is dephasing the vibrational coherence on the product electronic surface. However, the autocorrelation function is derived from the first-order limit of the correlation function in Eq. (8) which defines the time-dependent potential coupling. In perturbative calculations where obvious recurrences occur, the time-averaging operation is well defined and there is no need to invoke another operation which would mimic the solvent dephasing mechanisms (although without damping or dephasing no real rate constant exists).

Vastly different behavior is seen for nonperturbative calculations for bound electronic surfaces. The panels in Fig. 13 show the survival probability for the reactant population for the one-mode case for couplings of 500, 350, 200, and 50 cm^{-1} from top to bottom. The dashed curves give the golden rule rate and the dotted curves are the classic two-level system rate of $\cos^2(Vt/\hbar)$. For high potential couplings, the small high-frequency oscillations parallel the two-level rate. The short-time behavior, on average, does follow the golden rule rate. However, the system is still a coherent two-level system and the electronic coherence is not

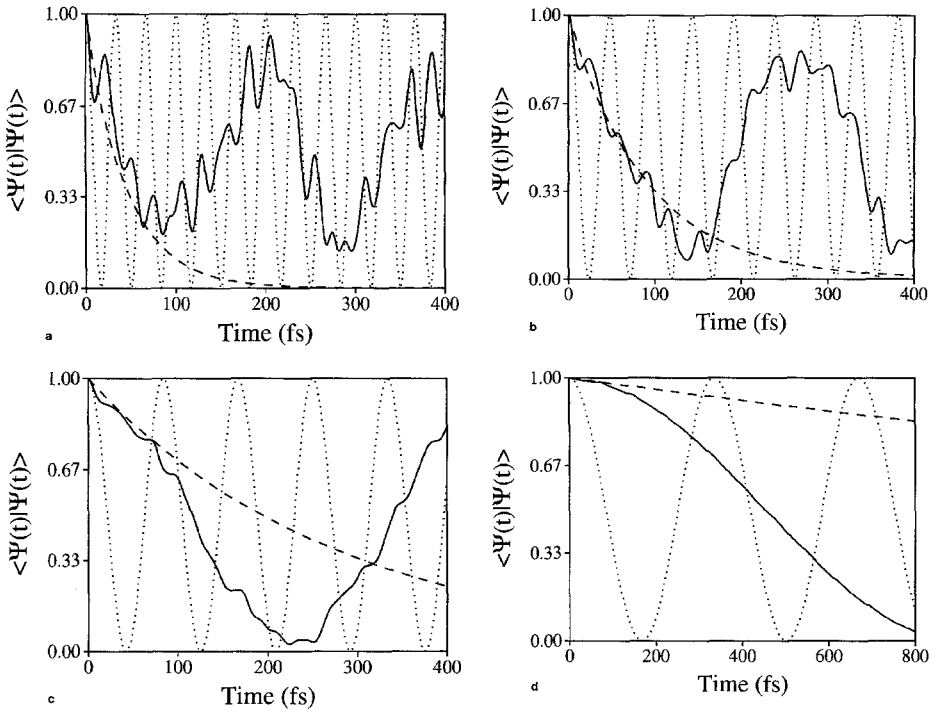

Fig. 13. Survival probability of the population on the reactant electronic surface for the one-mode system with potential couplings from top to bottom of 500, 350, 200, and 50 cm^{-1}

destroyed, only modulated. Upon increasing the number of modes two limiting forms of behavior can be observed: self-dephasing at higher couplings were the modulations decay to zero and steady-state behavior at lower couplings where constant populations are retained on the reactant and product surfaces. Nonzero values of ΔG^0 change the coupling range at which these appear.

5. Remarks

A substantive advantage of time-correlation function expressions for the electron transfer rate is that they permit going beyond the simple spin-boson golden rule model to include such important effects as nonequilibrium initial states [41] anharmonic vibrations, vibrational and electronic dephasing. Still, only a few actual calculations using these methods have appeared [5–7, 38, 41]. Since the integrals that give the rate coefficient are over a multimode correlation function, we generally expect rapid, essentially irreversible relaxation and dephasing, so that recurrences are unimportant and the short-time behavior of the correlation function is the only relevant part. Under these conditions, Gaussian wavepackets, and even frozen Gaussians, are adequate to describe the vibrational wavefunctions. This is no longer fully true when large-frequency changes occur, and it can fail badly for large anharmonicities (Sect. 4.1).

The golden rule itself is based on several assumptions, including little depletion of the initial-state population, a large effective density of final states, and a perturbative mixing that is in some sense small. Section 4.2 shows that for a simple two-state, one-mode model, short times and fairly weak coupling, the decay indeed follows the golden rule prediction at short times (little depletion). However, the real behavior is far more complicated, showing breaking of the original wavepacket, recurrences and virbrational modulations and frequencies. In a real situation, of course, other modes will couple, thermal coupling will occur, and dephasing processes will be crucial; these can be induced straightforwardly in the correlation function approach [11].

Acknowledgements. We are grateful to J. T. Hupp and to M. D. Todd for useful comments, and to the chemistry division of the ONR for support of this work. Mark Ratner thanks Jan Linderberg for a quarter century of instruction, inspiration and friendship.

References

1. Linderberg J, Öhrn Y (1972) Propagators in quantum chemistry. Academic Press, London
2. Kubo R, Tomita K (1954) Proc Phys Soc Japan 9:888; Kubo R (1965) in: Brittain WE (ed) Lectures in theoretical physics, Vol 1, Wiley, New York
3. Gordon RG (1968) Adv Mag Res 3:1
4. Heller ER (1978) J Chem Phys 68:2066; Heller ER (1981) Accts Chem Res 14:368; see also Schatz GC, Ratner MA (1993) Quantum mechanics in chemistry. Prentice-Hall, Englewood Cliffs, NJ, Chap 9
5. Borgis D, Hynes JT (1991) J Chem Phys 94:3619
6. Neria E, Nitzan A (1993) J Chem Phys 99:1109
7. Todd MD, Nitzan A, Ratner MA (1993) J Phys Chem 97:29
8. Hammerich AD, Kosloff R, Ratner MA (1992) J Chem Phys 97:6410; Hammerich AD, Manthe U, Kosloff R, Meyer H-D, Cederbaum LS, J Chem Phys (in press)
9. Islampour R, Alden RG, Wu GYC, Lin SH (1993) J Phys Chem 97:6793
10. Myers AB, Chem Phys 180:215
11. Hammerich AD, Nitzan A, Ratner MA (in preparation)
12. Linderberg J, Öhrn Y, Padkjaer SB (1985) J Chem Phys 91:4793; Linderberg J (1992) Int J Quant Chem 526:717
13. Kosloff R (1988) J Phys Chem 92:2987
14. Kosloff R Ann Revs Phys Chem (in press)
15. Leforestier C, Bisseling R, Cerjan C, Feit MD, Friesner R, Guldberg A, Hammerich AD, Jolicard G, Karrlein W, Meyer H-D, Lipkin N, Roncero O, Kosloff R (1991) J Comput Phys 94:59
16. Marcus RA, Revs Mod Phys 65: 599
17. Marcus RA, Sutin N (1985) Biochim Biophys Acta 811:265
18. Newton MD, Sutin N (1984) Ann Revs Phys Chem 35:437; Newton MD (1991) Chem Revs 91:767; Sutin N (1962) Ann Rev Nucl Sci 12:285
19. Mikkelsen KV, Ratner MA (1987) Chem Revs 87:113
20. De Vault D, Chance B (1966) Biophys J 6:825; De Vault D, Parkes JH, Chance B (1967) Nature (London) 215:642
21. Ulstrup J (1979) Charge transfer processes in condensed media. Springer, Berlin. Extensive early work on the spin-boson model is discussed, for example, by Garg A, Onuchic JN, Ambegoakar V (1985) J Chem Phys 83:4491
22. Schatz GC, Ratner MA (1993) Quantum mechanics in chemistry. Prentice-Hall, Englewood Cliffs, NJ, Chap 10.
23. Fischer SF, van Duyne RP (1977) Chem Phys 26:9
24. Jortner J (1976) J Chem Phys 64:4860
25. Hupp JT, Weaver M (1994) Naval research reviews 46:33

26. Ratner MA (1994) Naval research reviews 46:49
27. Brunschwig BS, Ehrenson S, Sutin N (1986) J Phys Chem 90:3657
28. Mikkelsen KV, Dalgaard E, Swanstrom P (1987) J Chem Phys 91: 3081
29. Marcus RA (1964) Ann Revs Phys Chem 15:155
30. Closs GL, Miller JR (1988) Science 240:440; Gould IR, Farid S (1993) J Phys Chem 97:13067
31. Sumi H, Marcus RA (1986) J Chem Phys 84:4894; Siddarth P, Marcus RA (1993) J Phys Chem 97:13078
32. Kosloff R, Tal-Ezer H (1986) Chem Phys Lett 127:233
33. Tal-Ezer H, Kosloff R, Cerjan C (1992) J Comput Phys 100:179
34. Brunschwig BS, Logan J, Newton MD, Sutin N (1980) J Am Chem Soc 102:5798
35. Siders P, Marcus RA, J Am Chem Soc 103:741
36. Hair N, Beattie J (1977) Inorg Chem 16:245
37. Marcus RA (1965) J Chem Phys 43:679
38. Todd MD, Nitzan A, Ratner MA, Hupp JT (1994) J Photochem Photobiol A82:87
39. Stynes HC, Ibers JA (1971) Inorg Chem 10:2304
40. Buhks E, Bixon M, Jortner J, Navon G (1979) Inorg Chem 18:2014
41. Coalson RD, Evans DG, Nitzan A (1994) J Chem Phys 101:436
42. Evans DG, Coalson RD (1993) J Chem Phys 99:6264